Numerical Investigation of High-lift Airfoil Fitted with Slat Cove Filler

Hasan Kamliya Jawahar*, Mahdi Azarpeyvand†,
University of Bristol, Bristol, United Kingdom, BS8 1TR
and
Carlos R. Ilário da Silva‡
Embraer, São José dos Campos, 12227-901, Brazil

Slat noise is well known as one of the dominant noise components of airframe noise. The slat cove has been demonstrated to be one of the primary sound source responsible for narrowband and broadband noise from high-lift devices. In order to reduce slat noise, several studies on slat cove fillers have been carried out in the past. In the present study Large Eddy Simulation with Dynamic Smagorinsky model has been used to assess the aerodynamic and aeroacoustic performance of a 30P30N high-lift airfoil with and without slat cove filler. The tests were carried out at an angle of attack of $\alpha = 5.5°$ at an inlet velocity of $U_\infty = 58$ m/s, corresponding to a chord-based Reynolds number of $Re_c = 1.71 \times 10^6$. The steady and unsteady pressure measurements validate well with the experimental data available in the literature. Contours of detailed flow field components such as mean velocity, turbulent kinetic energy and spanwise vorticity for both the baseline and slat cove filler configuration has been presented in a systematic manner. Contours of spanwise vorticity validate well with previous particle image velocimetry experimental measurements. Unsteady surface pressure spectra at various locations on the slat and main-element show that the application of slat cove filler eliminates the narrowband noise source and reduces the broadband noise for the tested cases. The pressure-velocity correlation results show us that the shear layer impingement on the slat lower surface contributes to the increase in low-mid frequency energy spectra. The use of slat cove filler eliminates the shear layer thus reducing the spectral levels at low-mid frequencies.

Nomenclature

c	=	stowed chord length, m
c_s	=	slat chord length, m
C_p	=	pressure coefficient
f	=	frequency, Hz
k	=	turbulent kinetic energy, m^2/s^2
l	=	span length, m
$L_x \times L_y \times L_z$	=	cell dimensions of computational grid
p_{ref}	=	reference pressure ($= 2 \times 10^{-5}$), Pa
Re_c	=	chord-based Reynolds number
U_∞	=	freestream velocity, m/s
U, V, W	=	time averaged velocity components, m/s
x, y, z	=	streamwise, spanwise and crosswise coordinates, m
y^+	=	dimensionless wall distance
α	=	angle of attack, °
$\gamma^2_{p_i p_j}$	=	coherence function
Φ_{pp}	=	wall-pressure power spectral density, Pa^2/Hz
Φ_{uu}	=	streamwise velocity power spectral density, dB/Hz
Φ_{vv}	=	crosswise velocity power spectral density, dB/Hz
ω_z	=	spanwise vorticity vector

*Research Associate, Department of Aerospace Engineering, hasan.kj@bristol.ac.uk
†Reader in Aeroacoustics, Department of Mechanical Engineering, m.azarpeyvand@bristol.ac.uk
‡Technology Development Engineer, Embraer, Sáo José dos Campos, Brazil, carlos.ilario@embraer.com.br

I. Introduction

THE introduction of high bypass-ratio turbofans engines into civil aircraft have drastically reduced engine noise over the last several decades, making the airframe noise the same magnitude as that of the engine noise, especially during the landing phase. In order to reduce these prominent airframe noise sources several fundamental passive and active flow control methods have been investigated over the recent years, such as, morphing structures [1–7], porous materials [8–11], surface treatments [12], serrations [13–15] and transverse jets [16]. One of the prominent sources of airframe noises are the high-lift devices namely the slats and flaps. Studies on conventional slat and wing configurations have shown that it mainly comprises of broadband and tonal noise components. Several studies on slat noise have shown several discrete tones at mid-frequency range [17–29]. However, their aeroacoustic mechanism is yet to be fully understood. These tonal peaks decrease with angle of attack but their amplitude decreases with increasing slat gap and overlap [24].

Several experimental and computational studies [30–33, 35, 39–47] were made over the past decade to asses and investigate the generation of the narrowband and broadband noise from the slat cove region. Some studies reduced the noise levels by filling the recirculation area within the slat cove filler. Even though a reduction in broadband noise was observed at all the instances it has been a challenge to maintain the aerodynamic performance of the high-lift device for the cove filled configurations. The slat cove filler profiles were derived from CFD analysis in order to maintain attached flow on the slat lower surface. From the experiments it was shown that slat cove filler was effective in reducing broadband slat noise up to 4-5 dB [30] that was measured using a microphone phased array. However, no aerodynamic measurements were presented in this study. Streett *et al.* further investigated the preliminary aerodynamic and acoustic performance of the SCF setup using trapezoidal wing swept model [31]. The study showed noise reduction to be sensitive to the angle of attack and SCF modification. The SCF modification showed a reduction of 3-5 dB over a wide spectrum. The aerodynamic performance appeared slightly better than the baseline at angles of attack below $\alpha = 20^\circ$ and stall occurred 2 degrees earlier compared to baseline. The specific reason for the aerodynamic performance loss was not pointed out due to the lack of aerodynamic data such as detailed surface pressure and wake shear layer measurements.

Imamura *et al.* and Ura *et al.* from JAXA showed experimentally and computationally [41, 43] that even though noise reduction can be achieved by the use of SCF, its profile significantly affects the aerodynamic lift characteristics of the three-element airfoil. They tested two SCF profiles that were designed based on the flow field streamlines of angles of attack $\alpha = 0^\circ$ and $\alpha = 8^\circ$ on an MDA 30P30N airfoil. Even though the results showed a reduction of 5 dB for both the cases they found that the aerodynamic lift characteristics performance were same as that of the baseline for only the SCF profile made from flow field streamlines of angle of attack 8° whereas the SCF profile made from angle of attack $\alpha = 0^\circ$ stalls prematurely. Tao and Sun [47] in a very recent optimization study performed several DES simulations using 44 configurations of SCF profile designs aimed to produce maximum lift coefficient for fixed design point with angle of attack of $\alpha = 22^\circ$ and $Re_c = 9 \times 10^6$. The final optimized SCF profile showed a reduction in noise while maintaining aerodynamic performance.

Kamliya Jawahar *et al.* [1–3] successfully carried out a comprehensive aerodynamic and aeroacoustic study using 30P30N airfoil fitted with two different types of slat cove fillers. The slat cove filler configuration showed similar overall aerodynamics performance as that of the baseline case and a slightly better aerodynamic performance at certain angles of attack. The study also showed that the characteristic narrowband peaks that arise from slat noise were eliminated by the application of the slat cove fillers for all the tested angle of attack. Moreover, the slat cove filler also showed a reduction in the broadband noise component at low-mid frequencies.

Several studies [1–3, 30–33, 41, 43–47] have shown the noise reduction capabilities of the slat cove filler. Even though the aerodynamic and aeroacoustic performance of slat cove fillers are well documented, the noise reduction mechanism of the slat cove fillers is yet to be identified. The current numerical study shows the aerodynamic performance characteristics such as surface pressure measurements, shear layer measurements, pressure-velocity coherence and the confluent boundary layers of all the three-element of the high-lift airfoil. Detailed mean and unsteady surface pressure results, velocity contours and turbulent kinetic energy around the slat cove region for the 30P30N airfoil with and without slat cove fillers are presented in a systematic manner. This will aid us to isolate and identify the noise reduction mechanism of the slat cove filler.

II. Computational Setup

Large Eddy Simulation (LES) to investigate the unsteady flow characteristics of 30P-30N airfoil were carried out. The airfoil had a retracted chord length of $c = 0.457$ m. The simulations were carried out at an angle of attack 5.5° for an inlet velocity of $U = 58$ m/s corresponding to a chord based Reynolds number of $Re_c = 1.71\times10^6$. Preliminary steady-state CFD RANS simulations were carried out with k-ω SST turbulence model and the validated results were used to initialize the LES simulation. Dynamic Smagorinsky subgrid-scale model [48] were used for all the presented LES simulations. A multi-block structured 3D gird for the MDA 30P-30N airfoil was created using ICEM CFD software. The computational setup was made with a domain size of $10c$ on the streamwise (x-$axis$) and crosswise (y-$axis$) direction (see Fig. 3) after a domain dependency study carried using domain sizes of $5c$, $10c$ and $20c$ and as suggested by BANC-III workshop [49]. The grid over all three elements was intended to be orthogonal to the airfoil surface. The close up view of the grid is shown in Figs. 1 and 2. The domain had a spanwise thickness (z-$axis$) of 0.025 m ($c/18$) which was deemed sufficient from the previous studies [35–38]. Periodic boundary condition on the span and no-slip boundary condition were used on the walls. The high-lift airfoils had a cell distribution of $L_x\times L_y\times L_z = 740\times60\times64$ in the near-field region. In the far-field region, the airfoil had a cell distribution of $L_x \times L_y \times L_z = 412 \times 146 \times 32$, respectively. LES mesh resolution requirement in the near wall cells in inner law scaling in the range of $\Delta x^+ \approx 100$, $\Delta y^+ \approx 1$ and $\Delta z^+ \approx 50$ close to the values suggested by Ewert and Manoha [50] were maintained. Each element of the multi-element airfoil was treated as an individual airfoil since the flow around all the elements were of high interest thus such densely meshed. The 2D grid consisted of a total number of 265,000 elements where all the existing grid dependency study has grid independent results from approximately 500,000 elements [34]. The final 3D LES mesh consisting of $\approx 11 \times 10^6$ cells. Each of the simulations was run on a cluster with 128 CPU cores for a period of 960 hours. The temporal duration of both the simulations was 0.26 s and the unsteady data were collected for the last 0.13 s.

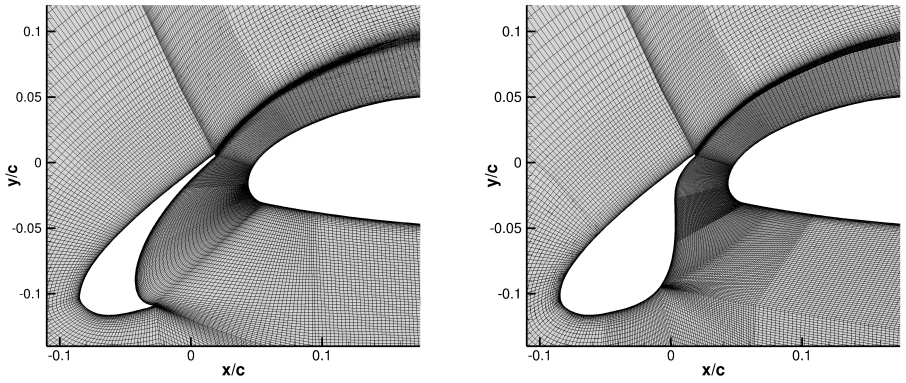

a) Baseline **b) Slat cove filler**

Fig. 1. Mesh distribution around the slat region for 30P30N high-lift airfoil.

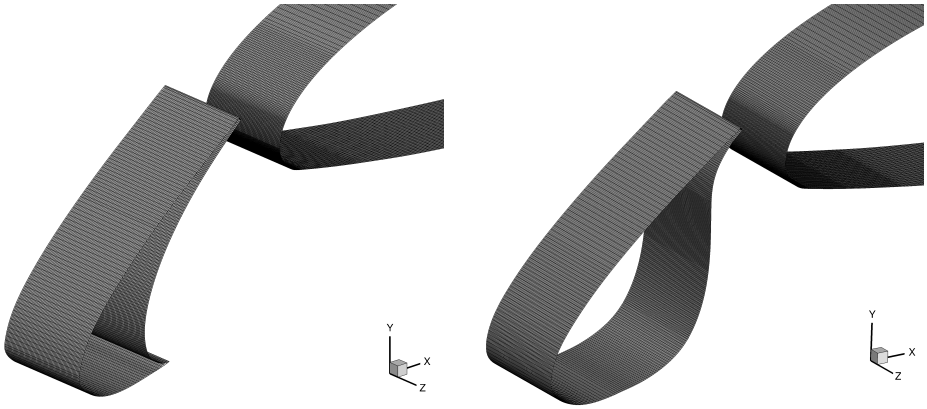

a) Baseline **b) Slat cove filler**

Fig. 2. Surface mesh around the slat region for 30P30N high-lift airfoil.

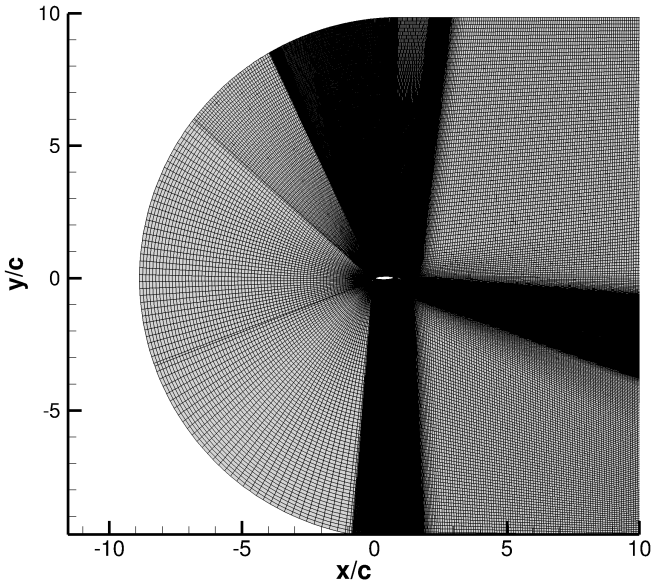

Fig. 3. Dense Mesh around 30P30N airfoil.

III. Results and Discussions

The time-averaged pressure coefficient C_p distribution results extracted along the mid-span of the computational domain for both the Baseline and SCF case are presented in Fig. 4. The simulations were carried out for an angle of attack $\alpha = 5.5^\circ$ at an inlet freestream velocity of $U_\infty = 58$ m/s corresponding to chord-based Reynolds number of $Re_c = 1.7 \times 10^6$. The results are compared against the Baseline experiment data produced by Murayama *et al.* [39] and the LES results have a good overall agreement with the experiments. The suction peak on the main element and the flap validate very well with the experimental data. The close-up view of the pressure distribution around the slat is shown in Fig. 4b and the simulation results are overpredicted by the simulation on the suction side of the slat at $x/c = 0.08$ by $\approx= 20\%$ relative to the experimental results. However, the LES results show a good overall agreement with the experimental results over the slat suction and pressure surfaces.

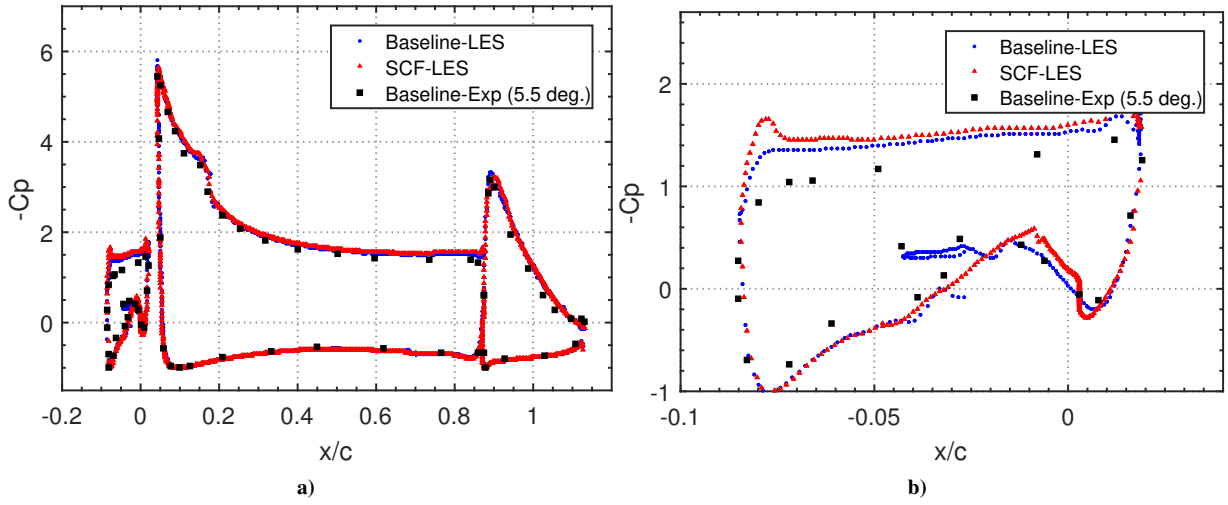

Fig. 4. Pressure distribution around the Baseline and SCF configuration compared with experimental data from Murayama *et al.* [39]

The contours of the average spanwise vorticity ($\omega_z c/U_\infty$) along the mid-span of the computational domain are

presented in Fig. 5 and the spanwise vorticity from PIV experiments carried out by Pascioni *et al.* [40] are presented in Fig. 6. The contour scales of the LES are set to have similar values as that of the PIV to have a better comparison. The average spanwise vorticity results of the LES are very similar to that of the PIV especially the reattachment location of the shear layer. This similarity enhances the reliability of the presented flow field contours within the slat cove region. The contours of normalized mean streamwise velocity (U/U_∞), crosswise velocity (V/U_∞) and turbulent kinetic energy (k/U_∞^2) at the mid-span location for both the Baseline and SCF are presented in Fig. 8. The flow features within the slat cove region are an important contributor to noise generation, especially the regions of the slat cusp shear layer and its impingement on the slat lower surface. The results of the streamwise velocity for the Baseline and the SCF configuration in Fig. 8a and b show negative velocity on the slat lower surface for the Baseline case, indicating the presence of recirculation within the slat cove region for the Baseline case. Moreover, the negative velocity in Fig. 8c and d are also seen in the crosswise velocity results within the slat cove region of the Baseline, which indicates the recirculation within the slat cove. The use of SCF clearly eliminates the recirculation region within the slat cove as the cove area is covered by the slat cove filler. The velocity contour plots also show that the SCF maintains the similar velocity magnitude relative to the Baseline at the slat gap region and over the main element. The contours of the turbulent kinetic energy in Fig. 8c and d show the elimination of the high turbulence kinetic energy within the slat cove region by the use of SCF and the results also show reduced turbulence kinetic energy magnitude at the slat wake region over the main element for the SCF compared to the Baseline.

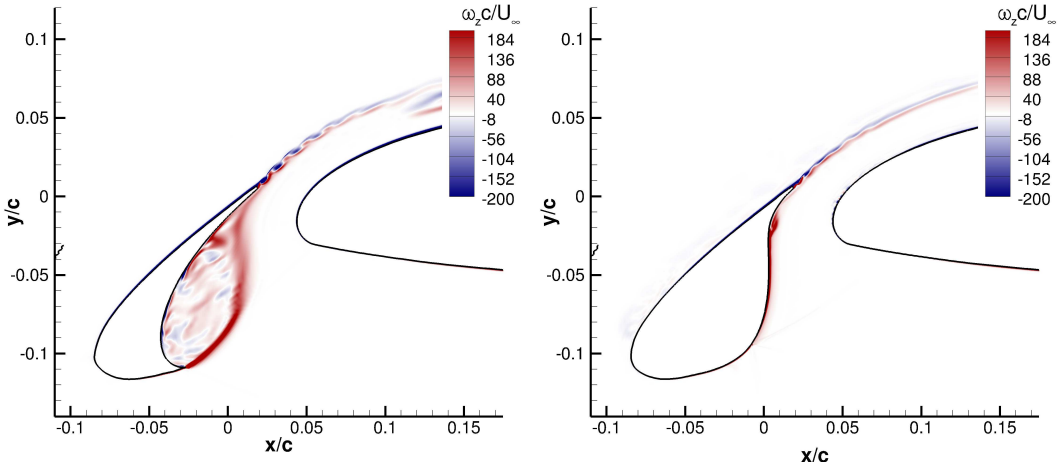

a) Baseline **b) Slat cove filler**

Fig. 5. Averaged contours of the normalized instantaneous spanwise vorticity, $\omega_z c/U_\infty$ for angle of attack $\alpha = 5.5$, $Re_c = 1.71 \times 10^6$ from LES.

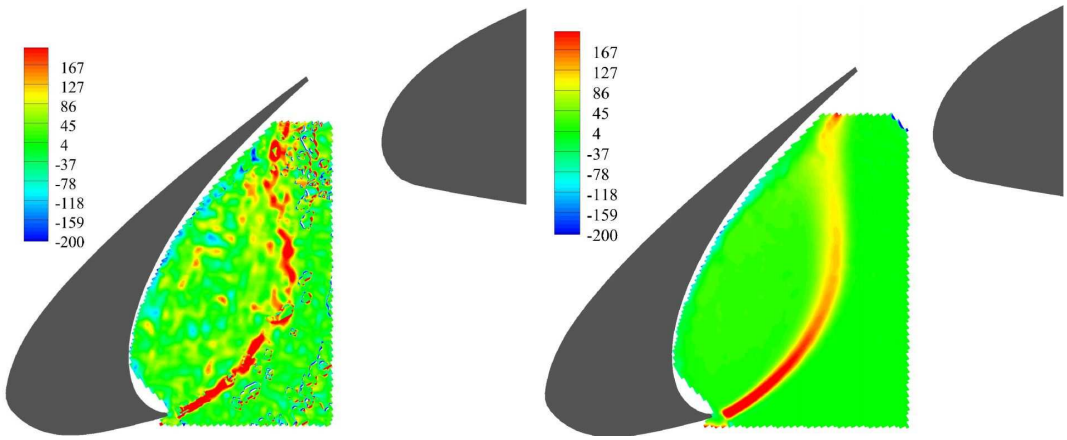

a) Instantaneous **b) Averaged**

Fig. 6. Contours of the spanwise vorticity, $\omega_z c/U_\infty$ for angle of attack $\alpha = 5.5$, $Re_c = 1.71 \times 10^6$ from PIV [40].

In order to have a detailed comparison between the Baseline and the SCF cases several line profile at various slat wake locations (see Table 1) and also at the various streamwise location on the suction side of the high lift airfoil (see Fig. 7) were extracted. The streamwise velocity profiles at the near wake location for both the Baseline and SCF showed insignificant differences for the wake deficit dip. The SCF showed reduced wake deficit at regions below the trailing edge for all the presented slat wake locations. The results show a significant reduction in turbulent kinetic energy for the SCF case relative to the Baseline case at all the presented slat wake location. The elimination of the unsteadiness within the slat cove region by the use of SCF has also reduced the unsteadiness at the slat wake region. The boundary layer profiles aft of the slat trailing edge just over the main-element and the flap are presented in Fig. 10. The mean streamwise velocity results at the location $x/c = 0.0575$ and 0.1057 show that the SCF has a slightly reduced slat wake velocity deficit relative to the Baseline. The effect of the slat wake is absent for the SCF at downstream locations $x/c = 0.2285$ and 0.6. The elimination of the slat cove vortices and streamlined profile of the SCF has resulted in increased streamwise velocity over the main-element for the SCF. The boundary layer profiles over the flap at locations $x/c = 0.8933$ and 1.0160 remain unchanged between the two cases.

Unsteady surface pressure plays a crucial role in the noise generated by the airfoil. The unsteady pressure and velocity from the simulation were logged at several measurement probes at the various chordwise location as depicted in Figs. 11 and 12. A total of 64 probes were evenly spread along the airfoil span at every chordwise measurement location. The unsteady spectral plots are presented only at the mid-span location for both the airfoils. The unsteady surface pressure data presented in Fig. 13 shows the comparison of the pressure spectral density (PSD) of the LES with experimental results from Murayama *et al.* [39]. The PSD of the pressure coefficient are presented for the slat pressure side close to trailing edge at location S_{L25} for the Baseline and S_{L31} for the SCF compared with the experimental measurements [39] available closest to the slat trailing edge on the pressure side. The computational results compare very well with the experimental results. The results for the baseline overpredicts the C_p spectra by $\approx$ 3 dB at low to mid-frequency range (200-1700 Hz). However, the simulations even predict the two narrowband peaks seen in the experiments at 1343 Hz and 1987 Hz. The results for the SCF show reduced broadband spectra up to $\approx$ 3 dB at low to mid-frequency range (100-1700 Hz) relative to the Baseline. The evolution of the surface pressure power spectral density (Φ_{pp}) normalized by the reference pressure ($p_{ref} = 2 \times 10^{-5}$ Pa) on the pressure side of the slat for both the SCF and Baseline cases are presented in Fig. 14. The Welch power spectral density of the pressure fluctuations were performed based on the time-domain LES pressure signals using Hamming windowing for segments of equal length with 50% overlap. In Fig. 14 the x-axis shows the normalized airfoil chord and the z-axis shows the slat based Strouhal number ($St_s = fc_s/U_\infty$). The 25 points used to calculate the pressure spectra are indicated in Fig. 11. The pressure spectra for the Baseline gradually increases closer to the trailing edge due to the impingement of the slat shear layer. For the SCF the pressure spectra on the slat pressure side show significant reduction compared to the Baseline case. The pressure spectra for the SCF increases after the flow separates on the lower surface at $x/c = 0.03$ yet still the spectral levels are much lower compared to the Baseline case. The tonal peak is seen at high frequencies $St_s < 15$ are associated with the vortex shedding from the blunt trailing edge and it has been observed in several other computational studies [36–38].

A critical observation of the spanwise coherence is required to asses the adequacy of the spanwise grid resolution and to also look into the spanwise distribution of the acoustic sources associated with the unsteady flow separation. In the current study the spanwise coherence function $\gamma^2_{p_i p_j}$ based on the fluctuating surface pressure are calculated using Eq. 1,

$$\gamma^2_{p_i p_j}(f) = \frac{|\ \Phi_{p_i p_j}(f)\ |^2}{\Phi_{p_i p_i}(f)\Phi_{p_j p_j}(f)} \quad \text{for } i = 1 \text{ and } j = 1, 2, 3, ..., \text{N}, \tag{1}$$

where the symbol $|\square|$ denotes the absolute value, N is the number of transducers along the span of the airfoil and $\Phi_{p_i p_j}$ is the cross-spectral density between two pressure signals p_i and p_j. The iso-coherence contours as a function of St_s and spanwise separation for the pressure side of the slat are presented in Figs. 15 and 16. The coherence at various St_s are presented in Fig. 17. Since periodic boundary condition has been employed the coherence can be calculated only for spanwise separation up to half the length of the computational span. The coherence drops rapidly with spanwise separation distance at all the presented $St_s = 0.5, 1, 5$. Therefore the present computational domain is sufficient enough to capture the unsteady flow separations within the slat cove.

The power spectral density of the unsteady streamwise and crosswise velocity (Φ_{uu}, Φ_{vv}) at various locations (see Fig. 12) are presented in Figs. 18, 19 and 20. The evolution of the streamwise and crosswise velocity spectra along the slat shear layer path for the Baseline is shown in Fig. 18. The PSD is plotted against St_s and S/S_{max}, where $S/S_{max} = 0$ at the slat cusp and $S/S_{max} = 1$ at the impingement location. The streamwise velocity spectra is increased at locations close to the slat cusp $S/S_{max} = 0 - 0.2$ and close to the impingement location $S/S_{max} = 0 - 0.1$. The evolution of the streamwise velocity spectra along the slat gap region for both the Baseline and SCF cases are presented in Fig. 19. The spectral levels of the streamwise velocity are higher at locations closer to the trailing edge (S_{G1}) compared to

the main-element (S_{G8}) for both the presented cases. For the Baseline case presented in Fig. 19a the spectral levels reduce by up to 30 dB at low Strouhal number at S_{G1} compared to S_{G8}. The SCF shows a decrease in the streamwise velocity spectra up to 20 dB compared to the Baseline at low Strouhal numbers ($St_s > 5$) at locations closer to the trailing edge (also see Figs. 21e and f). The reduction in velocity spectra for the SCF is due to the absence of the strong shear layer emanating from the slat cusp and its impingement at the slat trailing edge. The results clearly show the high-frequency tonal peak associated with the blunt trailing edge vortex shedding at $St_s = 17$ for the Baseline and $St_s = 20$ for the SCF. The change in St_s of the tonal peak between the Baseline and SCF is due to the absence of the unsteady shear layer impinging at the slat pressure side for the SCF case. The high-frequency tonal peak dissipates at locations closer to the main-element for the SCF. For the Baseline, the tonal component is prominent close to the slat trailing edge the energy of the spectra reduces at locations closer to the main-element but the tonal component is still visible. Overall, the velocity spectra close to the slat pressure side for the Baseline is higher than that of the SCF. The results for streamwise velocity spectra at the slat wake is presented in Fig. 20 for both the Baseline and SCF cases. The results show increased streamwise velocity spectral level at the vicinity of the trailing edge (S_{W1}) but at the location further away from the trailing edge the spectral levels decrease. The vortex shedding tonal peak is also seen very prominently at the vicinity of the trailing edge (S_{W1}) but the intensity of the tonal peak decreases for measurement probes at further downstream locations (S_{W8}). However, there is no prominent difference between the Baseline and SCF case for spectral levels at the slat wake. The results of the line plots extracted from various mid-span location from the pressure and velocity spectra evolution are presented in Fig. 21. The results clearly show increased spectral levels for the Baseline at mid Strouhal range ($St_s > 5$). At the slat gap location S_{G7} the SCF the vortex shedding tonal peak is not seen but a broadband increase at high Strouhal number.

The relationship between the pressure and velocity is necessary to investigate the influence of the surface pressure fluctuations with the separated shear layer. In order to capture this pressure-velocity coherence at various locations were presented in Figs. 22 and 23. The coherence between the unsteady surface pressure and velocity are calculated using Eq. 2,

$$\gamma^2_{p_i u_j}(f) = \frac{|\,\Phi_{p_i u_j}(f)\,|^2}{\Phi_{p_i p_i}(f)\Phi_{u_j u_j}(f)} \quad \text{for } i = 1 \text{ and } j = 1, 2, 3, ..., \mathrm{N}, \tag{2}$$

where N is the number of probes used for calculating the coherence and $\Phi_{p_i u_j}$ is the cross-spectral density between the pressure signal p_i and velocity signal u_j. The results for the pressure-velocity coherence for the slat shear layer path for the Baseline case is shown in Fig. 22. The results in Fig. 22a and c show the coherence between a pressure measurement probe on the slat cusp (S_{L0}) with the streamwise and crosswise velocity of the shear layer path (S/S_{max}), respectively. The results in Fig. 22b and d show the coherence between a pressure measurement probe at the flow impingement location on the slat pressure side (S_{L22}) with the streamwise and crosswise velocity of the shear layer path (S/S_{max}), respectively. The results show that the coherence between the pressure at the slat cusp and the shear layer with both the streamwise and crosswise velocity is high only at the low Strouhal range at the path location $S/S_{max} = 0 - 0.16$ of the shear layer path. Whereas, the results for the coherence between the pressure at the shear layer impingement location with streamwise velocity is much higher than that of the crosswise velocity and the coherence spectra are high for a larger path length. The results for the streamwise coherence is high for low-mid Strouhal range ($St_s < 1$) at path location $S/S_{max} = 0.4 - 0.76$ but for the crosswise coherence the regions of high coherence is found only between path location $S/S_{max} = 0.64 - 0.8$. The results here give us some insight into the broadband noise generation mechanism of the slat. The high coherence with the impingement location on the pressure side of the slat clearly shows us that the impingement of the shear layer contributes to the low-frequency broadband noise generation mechanism from the slat. The tonal peaks which are usually found in the experiments were found in the simulations only with a significantly lesser magnitude. However, the pressure-velocity coherence results have revealed the presence of the tonal peaks much more prominently, see Fig. 22b and d at $St_s \approx 0.7 - 1$.

The results for the pressure-velocity coherence between the slat pressure side impingement location and the slat gap streamwise velocity are presented in Fig. 23 for both the Baseline and SCF cases. The results show high coherence for the Baseline case for the slat cavity tonal peaks and the slat trailing edge vortex shedding tonal peak ($St_s < 10$) at all the slat gap locations. The SCF cases show high coherence only for the trailing edge vortex shedding tonal peak. These results show us that the tonal peaks are not present for the SCF compared to the Baseline and also that the tonal noise generation mechanism is highly related to the shear layer impingement region.

Table 1. Slat wake data extraction locations.

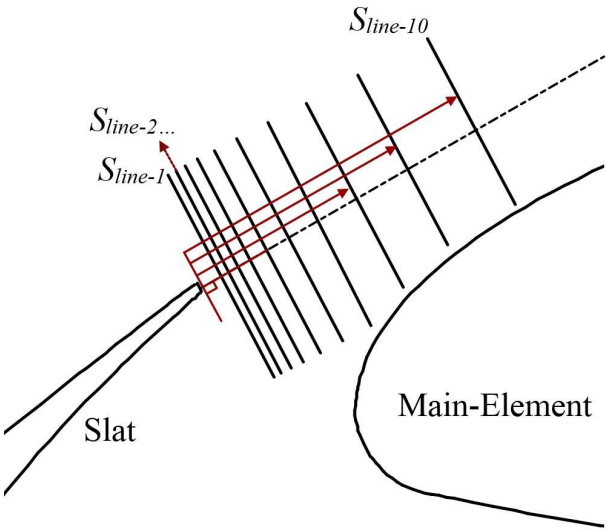

No.	x (mm)
S_{line-1}	15.0
S_{line-2}	19.9
S_{line-3}	26.5
S_{line-4}	35.3
S_{line-5}	46.9
S_{line-6}	62.4
S_{line-7}	82.9
S_{line-8}	110.3
S_{line-9}	147.0
$S_{line-10}$	195 .0

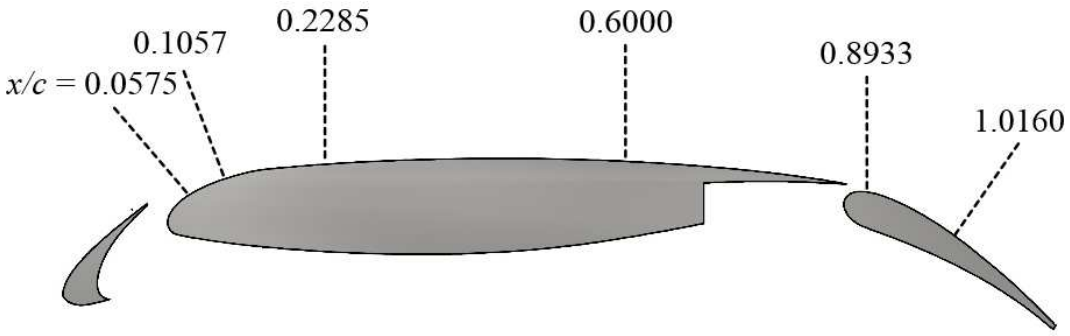

Fig. 7. Boundary layer measurement locations for the MDA 30P-30N airfoil.

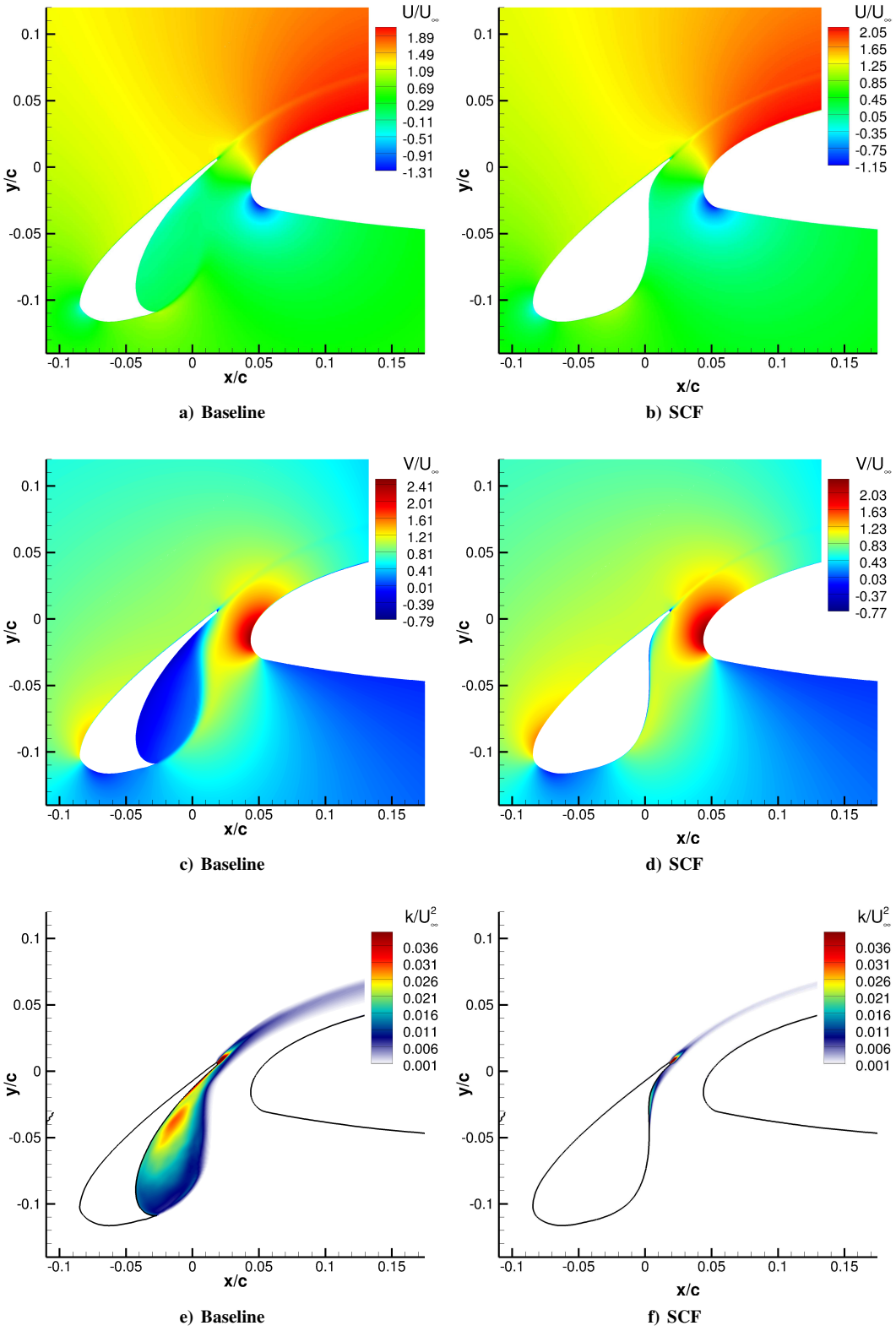

a) Baseline b) SCF

c) Baseline d) SCF

e) Baseline f) SCF

Fig. 8. Contours of the mean velocity components and turbulent kinetic energy around the slat region.

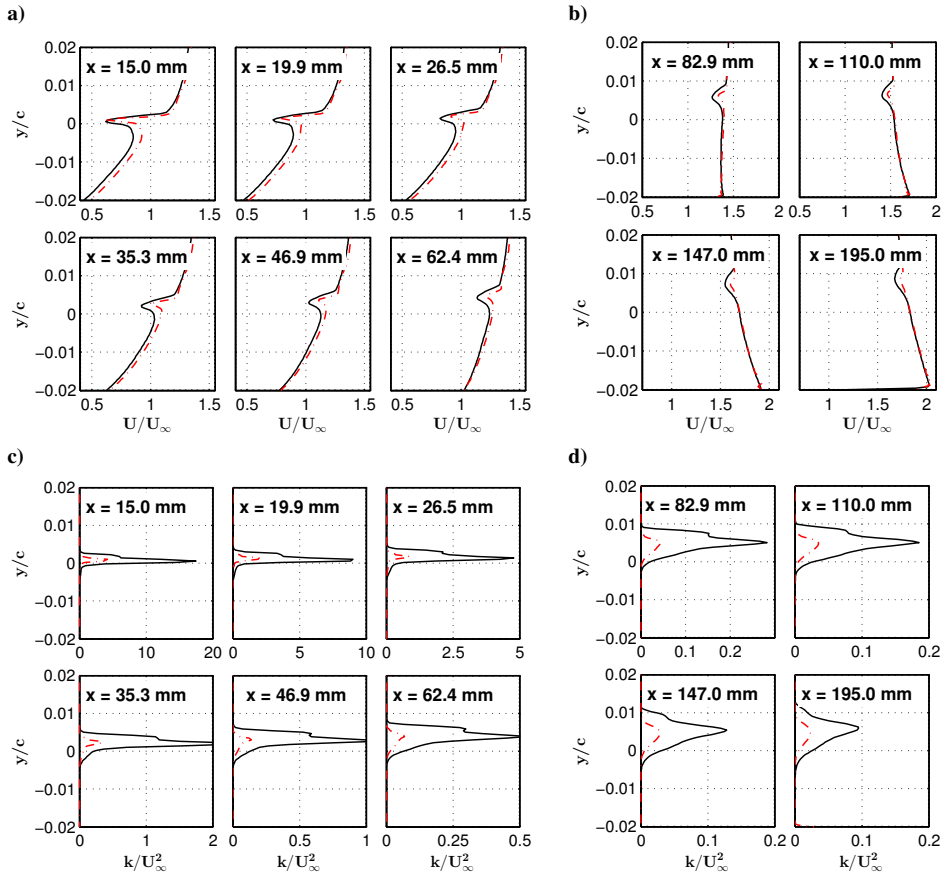

Fig. 9. Mean velocity and turbulent kinetic energy at the slat wake for Baseline — and SCF - . -.

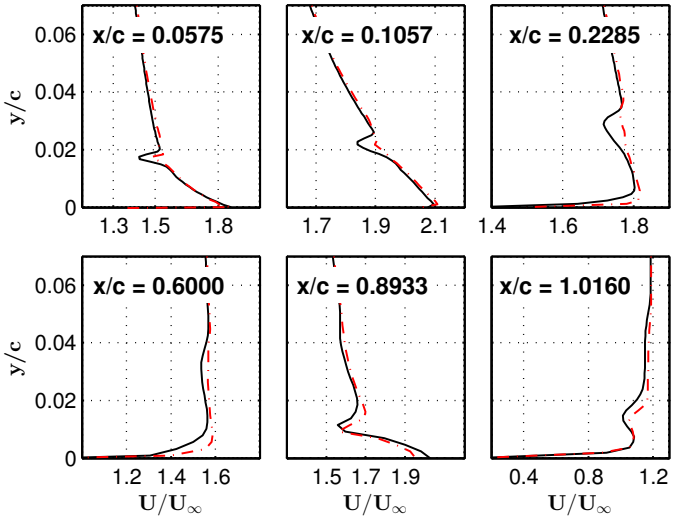

Fig. 10. Mean streamwise velocity profiles over the 30P30N airfoil for Baseline — and SCF - . -.

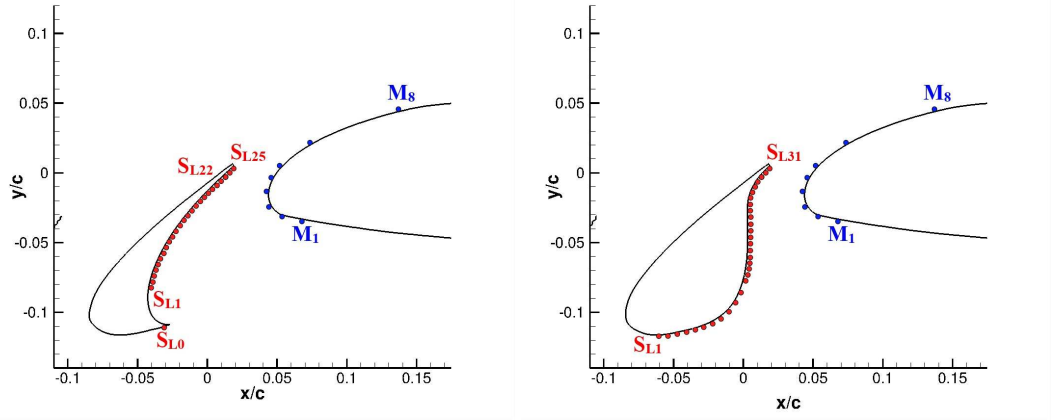

a) Baseline b) Slat cove filler

Fig. 11. Pressure probe locations for the Baseline and SCF configuration.

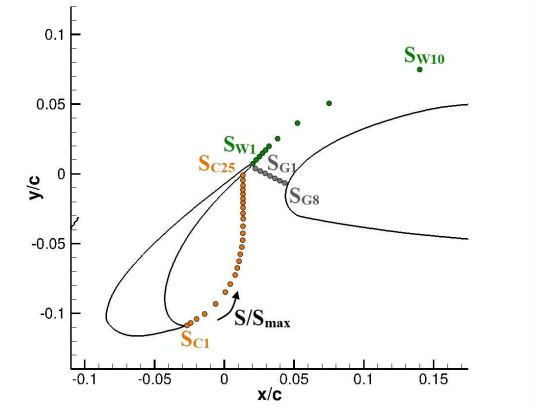

Fig. 12. Velocity probe locations for the Baseline and SCF configuration.

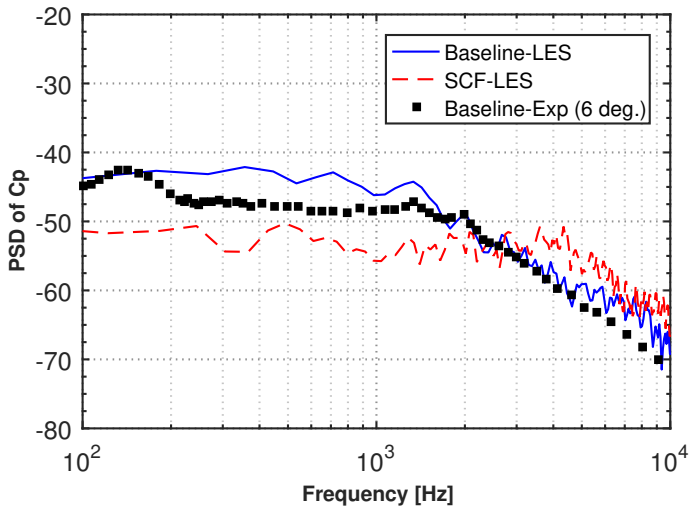

Fig. 13. Power spectral density of the pressure coefficient on the slat pressure side close to the trailing edge at location S_{L25} for Baseline and S_{L31} for SCF positions indicated in Fig. 11 compared with experimental data ($\alpha = 6°$) from Murayama *et al.* [39].

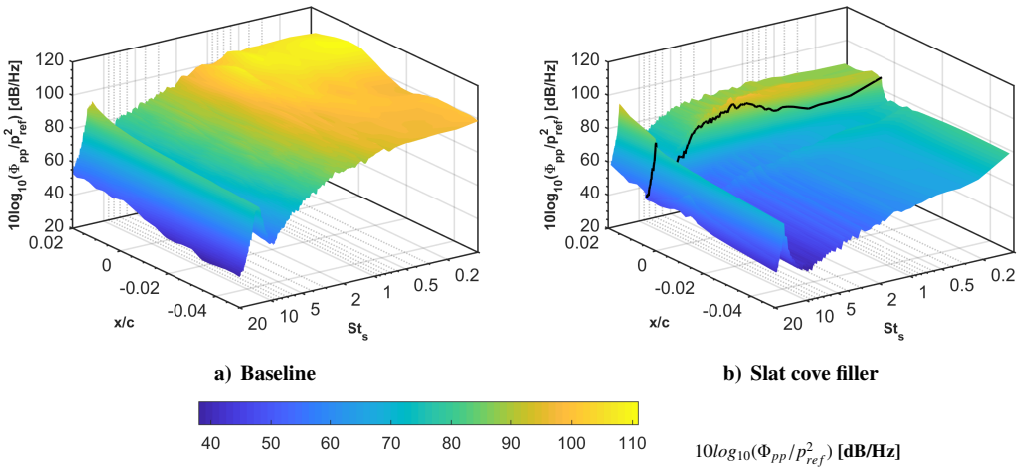

Fig. 14. Evolution of the wall-pressure spectra along the airfoil chord on the pressure side of the Slat with the flow separation region for the SCF (b) at $x = 0.03c$ indicated by —.

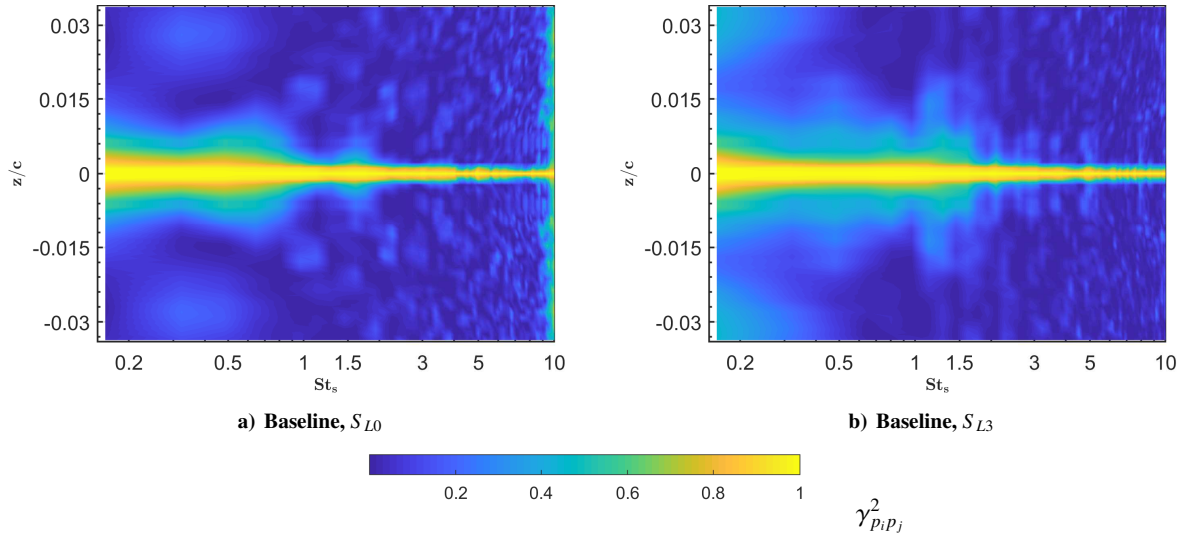

Fig. 15. Spanwise coherence of the fluctuating surface pressure at locations S_{L0} and S_{L3} for Baseline positions indicated in Fig. 11.

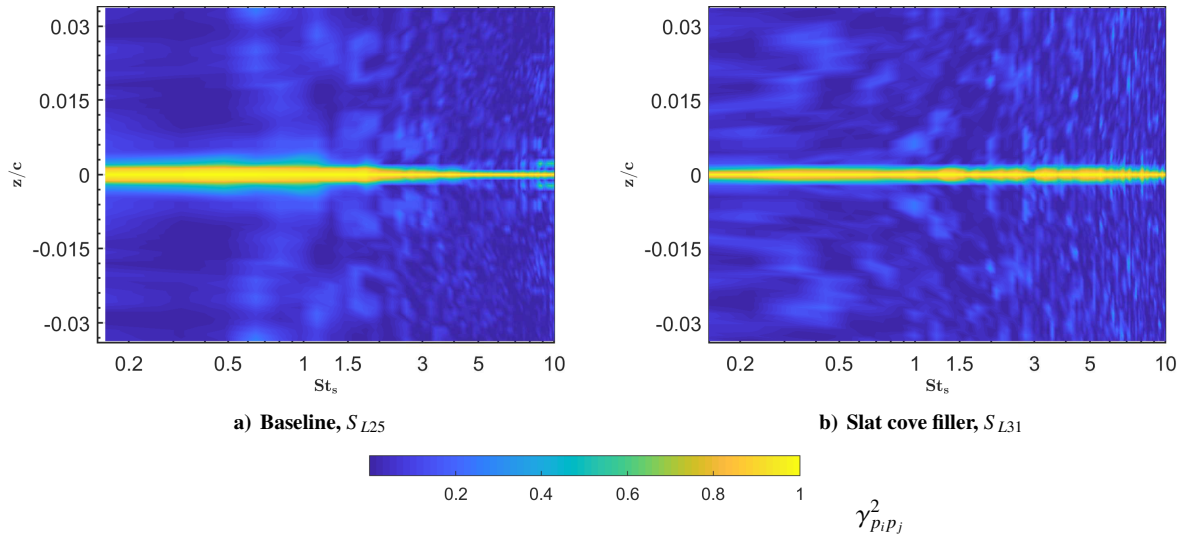

Fig. 16. Spanwise coherence of the fluctuating surface pressure at the trailing edge location S_{L25} for the Baseline and S_{L31} for SCF indicated in Fig. 11.

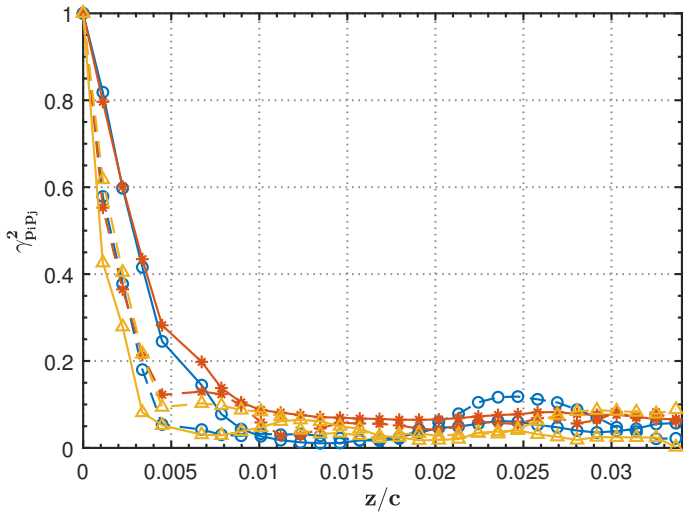

Fig. 17. Spanwise coherence of the surface pressure on the slat pressure side, at the trailing-edge location S_{L25} for Baseline (solid line) and at the location S_{L31} for SCF (dashed line) for $St_s = 0.5$ (circles) $St_s = 1$ (asterisk) and $St_s = 5$ (triangle).

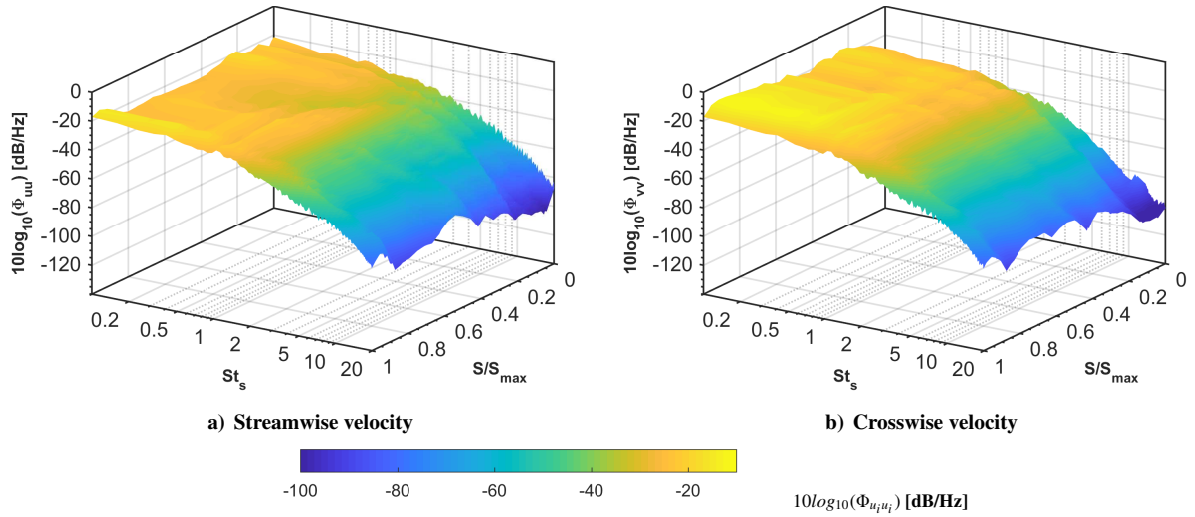

Fig. 18. Evolution of the streamwise and crosswise velocity spectra along the slat shear layer for the Baseline for points S_{C1} to S_{C25} indicated in Fig. 12.

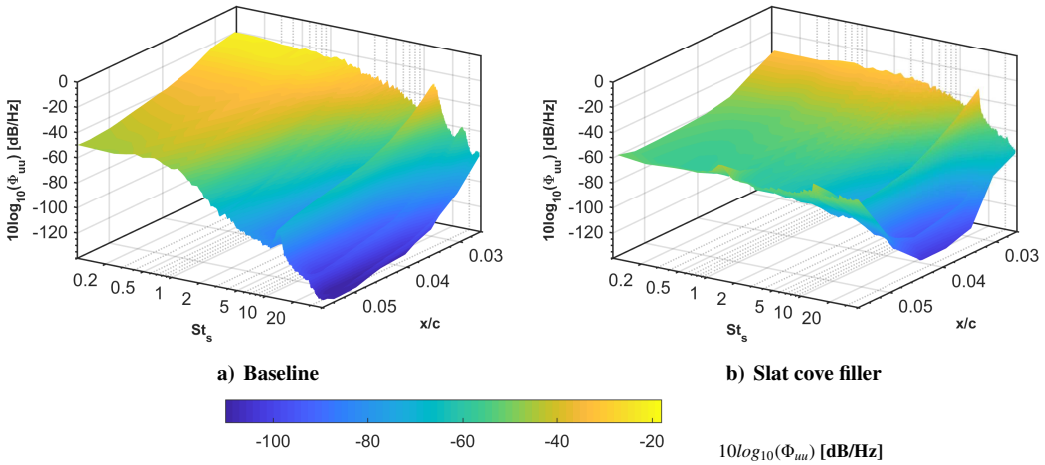

Fig. 19. Evolution of the streamwise velocity spectra along the slat gap region for both the Baseline and SCF configuration at points S_{G1} to S_{G8} indicated in Fig. 12.

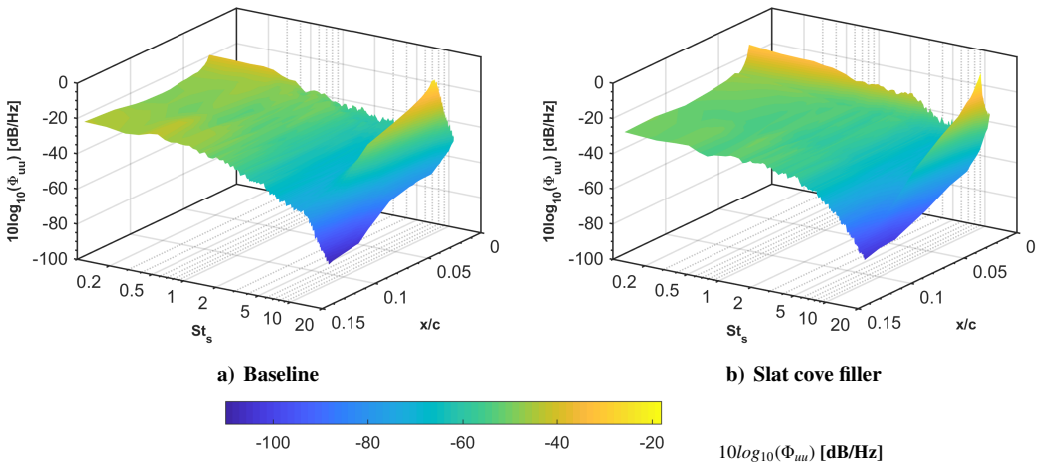

Fig. 20. Evolution of the streamwise velocity spectra along the slat wake region for both the Baseline and SCF configuration at points S_{W1} to S_{W8} indicated in Fig. 12.

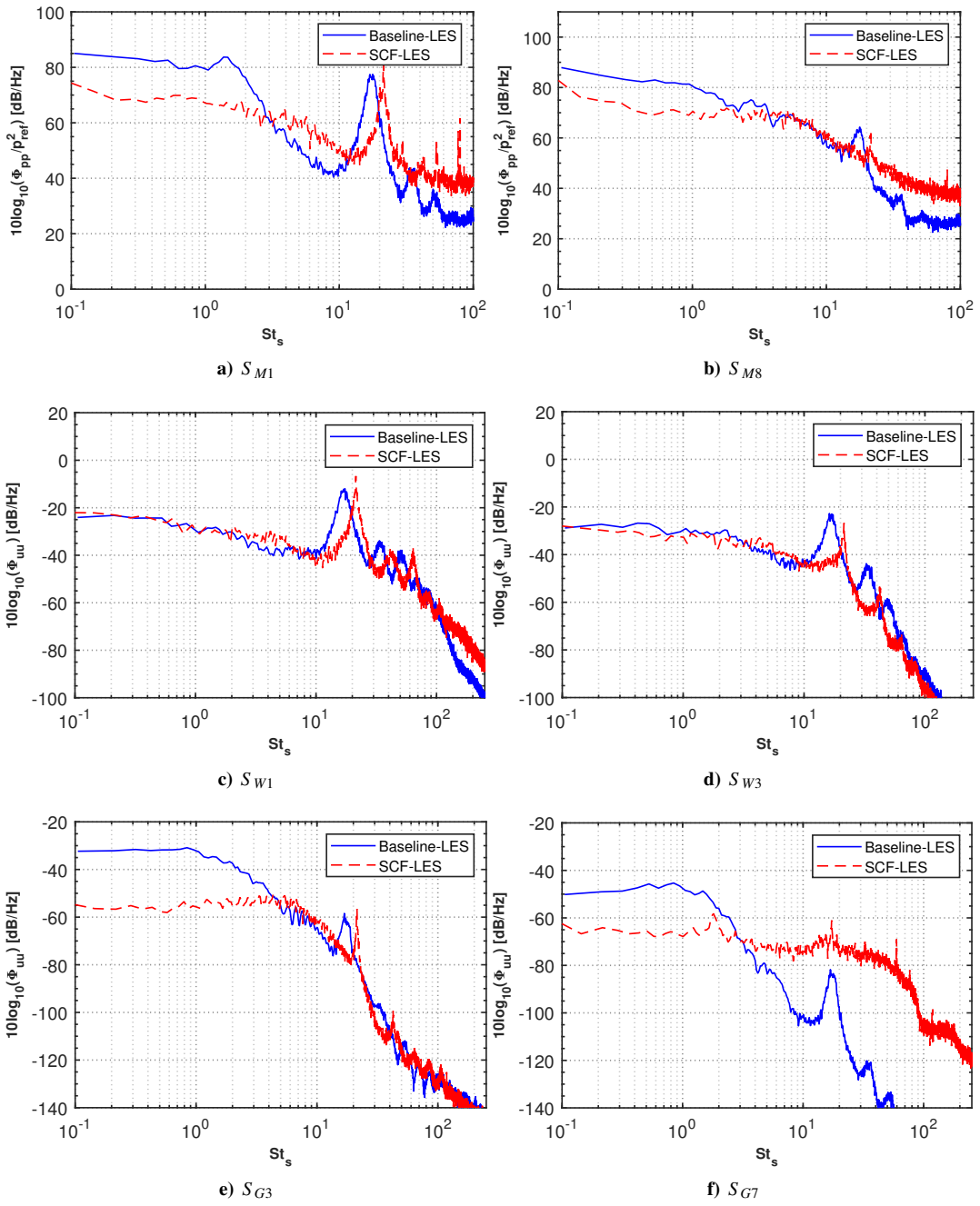

Fig. 21. Streamwise pressure (a,b) and velocity (c,d,e,f) spectra for both the Baseline and SCF configuration at various locations indicated in Figs. 11 and 12.

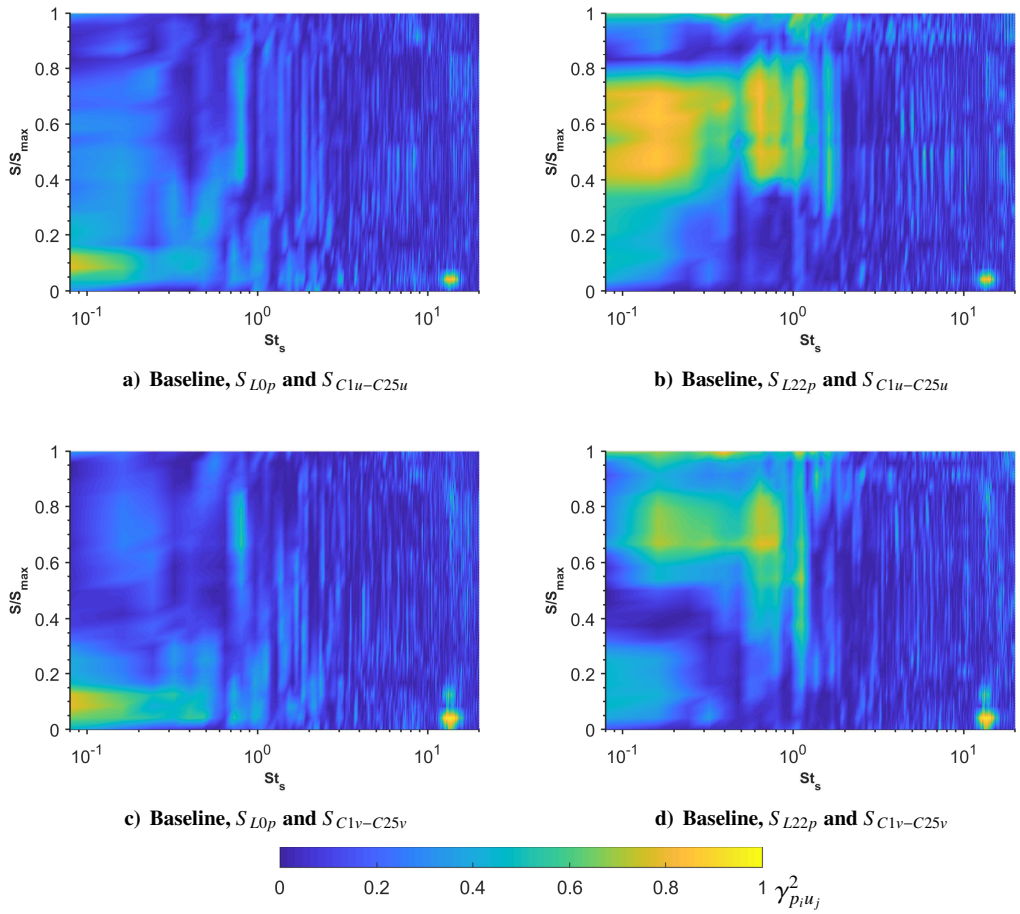

Fig. 22. Pressure velocity coherence between the slat cusp and the slat shear layer region for the Baseline configuration.

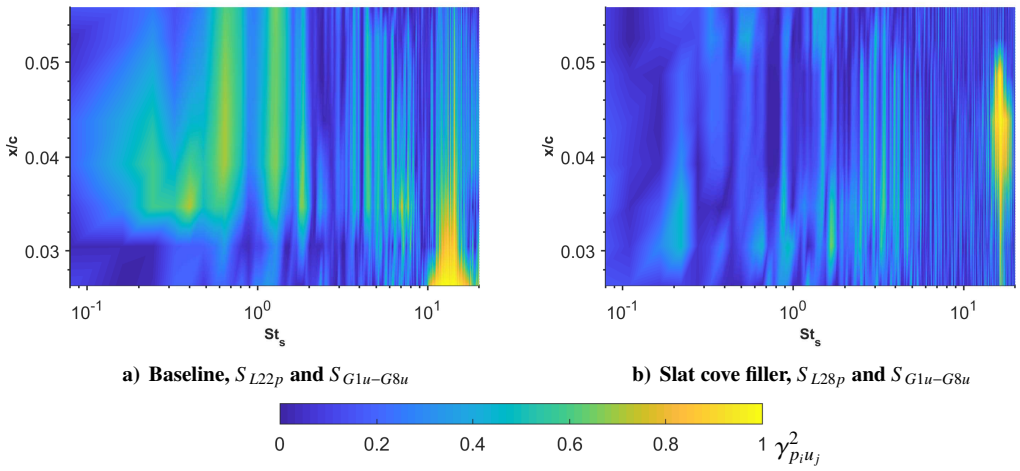

Fig. 23. Pressure velocity coherence between the slat pressure side and the slat gap region for the Baseline and SCF configuration.

IV. Conclusion

The aerodynamic and aeroacoustic performance of a 30P30N airfoil fitted with and without slat cove fillers (SCF) were investigated using numerical techniques. The airfoil was tested for a freestream velocity of $U_\infty = 58$ m/s, corresponding to the chord-based Reynolds number $Re_c = 1.71 \times 10^6$. The pressure distribution around the high-lift Baseline airfoil, unsteady pressure fluctuations and the spanwise vorticity contours validates well with existing experimental data set in the literature. The suction peak over the main element and the pressure distribution around the high-lift airfoil remained unchanged for the SCF configuration compared to the Baseline case. Detailed contour and line plots of the mean velocities, turbulent kinetic energy, and spanwise vorticity around the slat region are presented. The results clearly showed that the use of the slat cove filler completely eliminated the unsteady flow behavior that existed within the slat cove region. The results at the slat wake also showed reduced turbulent kinetic energy for the SCF relative to the Baseline. This is due to the elimination of the unsteady shear layer that impinges on the slat lower surface, which increases the energy at the slat wake for the Baseline. The unsteady surface pressure and shear layer velocity measurements were made at various location around the slat cove region. The spanwise coherence showed rapid drop confirming that the computational domain and the spanwise resolution was adequate enough for the current simulation. The Power spectral density (PSD) of the pressure and velocity at various locations were also calculated and presented in a systematic manner. The PSD of the pressure on the slat pressure surface showed that reduced pressure spectra for the SCF compared to the Baseline case. The PSD of the velocity in the slat gap region also showed reduced velocity spectra for the SCF. A tonal peak at high frequency ($St_s > 15$) was present for both the cases, which is associated with the blunt trailing edge vortex shedding as seen and discussed in available studies in the literature. The results for pressure-velocity coherence were calculated to further understand the relation between the surface pressure and the unsteady slat shear layer. The pressure-velocity coherence results showed increased streamwise velocity spectra at low-mid frequency range closer to the slat shear layer impingement region. Overall the results have shown that the application of SCF maintains the aerodynamic performance of the high-lift airfoil while reducing the energy content of the near-field pressure fluctuations.

References

[1] Kamliya Jawahar, H., Azarpeyvand, M., and Carlos R.Ilario., "Aerodynamic and Aeroacoustic Performance of Three-element High Lift Airfoil fitted with Various Cove Fillers", AIAA 2018-3142, 2018.

[2] Kamliya Jawahar, H., Showkat Ali, S. A., Azarpeyvand, M., and Carlos R.Ilario., "Aeroacoustic Performance of Three-element High Lift Airfoil with Slat Cove Fillers", 25th AIAA/CEAS Aeroacoustic conference, Delft University of Technology, Netherlands, 2019.

[3] Kamliya Jawahar, H., Azarpeyvand, M., and Carlos R.Ilario. "Experimental Investigation of Flow Around Three-element High-lift Airfoil with Morphing Fillers", AIAA 2017-3364, 2017.

[4] Ai, Q., Kamliya Jawahar, H., and Azarpeyvand, M., "Experimental Investigation of Aerodynamic Performance of Airfoils Fitted with Morphing Trailing Edges", AIAA 2016-1563, 2016.

[5] Kamliya Jawahar, H., Ai, Q., and Azarpeyvand, M., "Experimental and Numerical Investigation of Aerodynamic Performance of Airfoils Fitted with Morphing Trailing Edges", AIAA 2017-3371, 2017.

[6] Kamliya Jawahar, H., Azarpeyvand, M., and Silva, C., "Aerodynamic and Aeroacoustic Performance of Airfoils Fitted with Morphing Trailing-edges", AIAA 2018-2815, 2018.

[7] Kamliya Jawahar, H., Ai, Q., and Azarpeyvand, M., "Experimental and Numerical Investigation of Aerodynamic Performance of Airfoils with Morphed Trailing Edges", *Renewable Energy*, Vol. 127, 2018, pp. 355-367.

[8] Liu, H.R., Azarpeyvand, M., Wei, J.J., and Qu, Z.G., "Tandem Cylinder Aerodynamic Sound Control Using Porous Coating", *Journal of Sound and Vibration*, Vol. 334, 2015, pp. 190-201.

[9] Showkat Ali, S. A., Azarpeyvand, M., and Ilario, C., "Trailing Edge Flow and Noise Control using Porous Treatments", *Journal of Fluid Mechanics*, Vol. 850, 2018, pp. 83-119.

[10] Showkat Ali, S. A., Szoke, M., Azarpeyvand, M., and Ilario, C., "Turbulent Flow Interaction with Porous Surfaces", AIAA 2018-2801, 2018.

[11] Showkat Ali, S. A., Azarpeyvand, M., Szoke, M. and da Silva, C. R. I., "Boundary layer flow interaction with a permeable wall," *Physics of Fluids*, Vol. 30, 2018, pp. 085111.

[12] Afshari, A., Azarpeyvand, M., Dehghan, A. A., and Szoke, M., "Trailing Edge Noise Reduction Using Novel Surface Treatments", AIAA 2016-2834, 2016.

[13] Liu, X., Kamliya Jawahar, H., Azarpeyvand, M., and Theunissen, R. "Aerodynamic Performance and Wake Development of Airfoils with Serrated Trailing Edges", *AIAA Journal*, Vol. 55, No. 11, 2017, pp. 3669-3680.

[14] Lyu, B., Azarpeyvand, M., and Sinayoko, S., "Prediction of Noise from Serrated Trailing Edges", *Journal of Fluid Mechanics*, Vol. 793, 2016, pp. 556-588.

[15] Mayer, Y. D., Lyu, B., Kamliya Jawahar, H., and Azarpeyvand, M., "A Semi-analytical Noise Prediction Model for Airfoils with Serrated Trailing Edges", *Renewable Energy (in press)*, 2019.

[16] Szoke, M., Fiscaletti, D., and Azarpeyvand, M., "Effect of Inclined Transverse Jets on Trailing-edge Noise Generation," *Physics of Fluids*, Vol. 30, 2018, pp. 085110.

[17] Roger, M., and Perennes, S., "Low-Frequency Noise Source in Two Dimensional High-lift Devices", AIAA 2000-1972, 2000.

[18] Kolb, A., Faulhaber, P., Drobietz, R., and Grunewald, M., "Aeroacoustic Wind Turbine Measurements on a 2D High-lift Configuration", AIAA 2007-3447, 2007.

[19] Mendoza, J.M., Brooks, T.F., and Humphreys, W.M., "An Aeroacoustic Study of a Leading Edge Slat Configuration", *international Journal of Aeroacoustics*, Vol. 1, No. 3, 2002, pp. 241-274.

[20] Hein, S., Hohage, T., Koch, W., and Schoberl, J., "Acoustic Resonances in a High-lift Configuration", *Journal of Fluid Mechanics*, Vol. 582, pp: 179-202, 2007.

[21] Makiya, Sanehiro., Inasawa, A., and Asai, M., "Vortex Shedding and Noise Radiation from a Slat Trailing Edge", *AIAA Journal*, Vol. 48, No. 2, 2010, pp: 502-508.

[22] Terracol, M., Manoha, E., and Lemoine, B., "Investigation of the Unsteady Flow and Noise Generation in a Slat Cove", *AIAA Journal*, Vol. 54, No. 2, 2016, pp: 469-489.

[23] Pagani, C. C., Souza, D. S., and Medeiros, M. F., "Slat Noise: Aeroacoustic Beamforming in Closed-Section Wind Tunnel with Numerical Comparison", *AIAA Journal*, Vol. 54, No. 7, 2016, pp: 2100-2115.

[24] Pagani, C. C., Souza, D. S., and Medeiros, M. F., "Experimental Investigation on the Effect of Slat Geometrical Configuration on Aerodynamic Noise", *Journal of Sound and Vibration*, Vol. 394, pp: 256-279, 2017.

[25] Pascioni, K. A., and Cattafesta, L. N., "An Aeroacoustic Study of a Leading-edge Slat: Beamforming and Far-field Estimation using Near-field Quantities", *Journal of Sound and Vibration*, Vol. 429, pp: 224-244, 2018.

[26] Li, L., Liu, P., Guo, H., Hou, Y., Geng, X., and Wang, J., "Aeroacoustic Measurement of 30P30N High-lift Configuration in the Test Section with Kevlar Cloth and Perforated Plate", *Aerospace Science and Technology*, Vol. 70, pp: 590-599, 2017.

[27] Li, L., Liu, P., Guo, H., Geng, X., Hou, Y., and Wang, J., "Aerodynamic and Aeroacoustic Experimental Investigation of 30P30N High-lift Configuration", *Applied Acoustics*, Vol. 132, pp: 43-48, 2018.

[28] Li, L., Liu, P., Xing, Y., and Guo, H., "Time-frequency Analysis of Acoustic Signals from a High-lift Configuration with two Wavelet Functions", *Applied Acoustics*, Vol. 129, pp: 155-160, 2018.

[29] Li, L., Liu, P., Xing, Y., and Guo, H., "Wavelet Analysis of the Far-Field Sound Pressure Signals Generated from a High-lift Configuration", *AIAA Journal*, Vol. 56, No.1 pp: 432-437, 2018.

[30] Horne, W. C., James, K. D., Arledge, T. K., Soderman, P. T., Field, M., Burnside, N., and Jaeger, S. M., "Measurement of 26%-scale 777 Airframe Noise in the NASA Ames 40- by 80 foot Wind Tunnel", AIAA 2005-2810, 2005.

[31] Streett, C., Casper, J., Lockard, D., Khorrami, M., Stoker, R., Elkoby, R., Wenneman, W., and Underbrink, J., "Aerodynamic Noise Reduction for High-Lift Devices on a Swept Wing Model", AIAA 2006-212, 2006.

[32] Andreou, C., Graham, W., Shin, H. C., Street, T., Member, S., and Lecturer, S., "Aeroacoustic study of airfoil leading edge high-lift devices", AIAA 2006-2515, 2006.

[33] Andreou, C., Graham, W., Shin, H.-c., Introduction, I., Street, T., Member, S., and Lecturer, S., "Aeroacoustic Comparison of Airfoil Leading Edge High-Lift Geometries and Supports", AIAA 2007-230, 2007.

[34] Fang, L., "Suppression of Stall on High-camber Flap Using Upper-surface Blowing", MSc Research, Cranfield University, pp: 1-107, 2011.

[35] Choudhari, M. M., and Khorrami, M. R., "Effect of Three-dimensional Shear-layer Structures on Slat Cove Unsteadiness", *AIAA Journal*, Vol. 45, No.9 pp: 2174-2186, 2007.

[36] Lockard, D. P., and Choudhari, M. M., "Noise Radiation from a Leading-Edge Slat", AIAA 2009-3101, 2009.

[37] Lockard, D. P., Choudhari, M. M., and Buning, P. G., "Grid Sensitivity Study for Slat Noise Simulations", AIAA 2014-2627, 2014.

[38] Lockard, D. P., Choudhari, M. M., and Buning, P. G., "Influence of Spanwise Boundary Conditions on Slat Noise Simulations", AIAA 2015-3136, 2015.

[39] Murayama, M., Nakakita, K., Yamamoto, K., Ura, H., and Ito, Y., "Experimental Study of Slat Noise from 30P30N Three-Element High-Lift Airfoil in JAXA Hard-Wall Low-Speed Wind Tunnel", AIAA 2014-2080, 2014.

[40] Pascioni, K. A., Cattafesta, L. N., and Choudhari, M. M., "An Experimental Investigation of the 30P30N Multi-Element High-Lift Airfoil", AIAA 2014-3062, 2014.

[41] Imamura, T., Ura, H., Yokokawa, Y., Enomoto, S., Yamamoto, K., and Hirai, T., "Designing of Slat Cove Filler as a Noise Reduction Device for Leading-edge Slat", AIAA 2007-3473, 2007.

[42] Imamura, T., Ura, H., Yokokawa, Y., Enomoto, S., Yamamoto, K., and Hirai, T., "A Far-field Noise and Near-field Unsteadiness of a Simplified High-lift-configuration Model (Slat)", AIAA 2009-1239, 2009.

[43] Ura, H., Yokokawa, Y., Imamura, T., Ito, T., and Yamamoto, K., "Investigation of Airframe Noise from High Lift Configuration Model", AIAA 2008-19, 2008.

[44] Shmilovich, A., Yadlin, Y., and Pitera, D. M., "Wing Leading Edge Concepts for Noise Reduction", 27th International Congress of the Aeronautical Sciences (ICAS), 2010.

[45] Shmilovich, A., Yadlin, Y., and Company, T. B., "High-lift Systems for Enhanced Take-off Performance", 28th International Congress of the Aeronautical Sciences, 2012, pp. 1-13.

[46] Scholten, W. D., Hartl, D. J., Turner, T. L., and Kidd, R. T., "Development and Analysis-Driven Optimization of Superelastic Slat-Cove Fillers for Airframe Noise Reduction", *AIAA Journal*, dec 2015, pp. 1-17.

[47] Tao, J. and Sun, G., "A Novel Optimization Method for Maintaining Aerodynamic Performances in Noise Reduction Design", Aerospace Science and Technology, Vol. 43, 2015, pp. 415-422.

[48] Lilly D. K., "A Proposed Modification of the Germano Subgrid-Scale Closure Method.", *Physics of Fluids*, Vol. 4, 1992, pp: 633-635.

[49] Choudhari, M., and Lockard, D. P., and BANC-III Category-7 Team, "Assessment of Slat Noise Predictions for 30P30N High-Lift Configuration from BANC-III Workshop," 21st AIAA/CEAS Aeroacoustics Conference, AIAA Paper 2015-2844, 2015.

[50] Wagner, C., Huttl, T., and Pierre, S., *Large-eddy Simulation for Acoustics.*, Cambridge University Press, Vol. 20, No.11 pp: 956-963, 2007.

[51] Garcia-Sagrado, A. and Hynes, T., "Wall-Pressure Sources Near an Airfoil Trailing Edge Under Separated Laminar Boundary Layers", *AIAA Journal*, Vol. 49, No. 9, 2011, pp. 1841-1856.

[52] Garcia-Sagrado, A. and Hynes, T., "Stochastic Estimation of Flow near the Trailing Edge of a NACA0012 Airfoil", *Experiments in Fluids*, Vol. 51, No. 4, 2011, pp. 1057-1071.

[53] Garcia-Sagrado, A. and Hynes, T., "Wall Pressure Sources Near an Airfoil Trailing Edge Under Turbulent Boundary Layers", *Journal of Fluids and Structures*, Vol. 30, 2012, pp. 3-34.

[54] Valarezo, W. O., "High-lift testing at high Reynolds numbers", AIAA-92-3986, 1992.

[55] Valarezo, W. O., Dominik, C. J., and Mcghee, R. J., "Reynolds and Mach number Effects on Multielement Airfoils", N93-27446, 1992.

[56] Chin, V. D., Peters, D.W., Sdaid, F.W., and Mcghee, R. J., "Flowfield Measurements About a Multi-Element Airfoil At High Reynolds Numbers", AIAA-93-3137, 1993.

[57] Olson, S., Thomas, F., and Nelson, R., "A Preliminary Investigation into Slat Noise Production Mechanisms in a High-lift Configuration", AIAA 2000-4508, 2000.